



## Failure properties of rocks in true triaxial unloading compressive test

Kun DU<sup>1</sup>, Xi-bing LI<sup>2</sup>, Di-yuan LI<sup>2</sup>, Lei WENG<sup>2</sup>

1. Advanced Research Center, Central South University, Changsha 410083, China;
2. School of Resources and Safety Engineering, Central South University, Changsha 410083, China

Received 13 January 2014; accepted 28 June 2014

**Abstract:** Slabbing failure often occurs in the surround rock near a deep underground excavation. The mechanism of slabbing failure is still unclear. In order to reveal the influence of the intermediate principal stress ( $\sigma_2$ ) on slabbing failure, true triaxial unloading compressive test was carried out based on the stress path of the underground engineering excavation, i.e., unloading the minimum principal stress ( $\sigma_3$ ), keeping  $\sigma_2$ , increasing the maximum principal stress ( $\sigma_1$ ). The initiation and the propagation of slabbing fracture in rock specimens were identified by examining the acoustic emission (AE) and the infrared radiation characterization. The test results show that the failure modes of the granite and red sandstone specimens are changed from shear to slabbing with the increase of  $\sigma_2$ . The AE characteristic of rock specimen under low  $\sigma_2$  is swarm type which is the main shock type under high  $\sigma_2$ . The infrared radiation properties of rock specimen under different  $\sigma_2$  are also different. The temperature change area is just along the shear fracture such as the uniaxial compression. With the increase of  $\sigma_2$ , the temperature change area is planar of rock specimen which proves that the failure mode of rock specimen turns into slabbing.

**Key words:** true triaxial stress; unloading; slabbing; acoustic emission; infrared radiation

### 1 Introduction

The mining depths of a number of underground metal mines have reached or exceeded 1000 m in China [1]. With the increase of mining depth, the vertical in-situ stress was reported to increase about 27 kPa/m [2]. These mines with a high mining depth encounter a series of engineering problems induced by high in-situ stress. The stress condition of surrounding rock mass changes related to the engineering excavation unloading process. Generally, it may change from true triaxial stress condition to biaxial or even one dimensional stress condition. Afterwards, the rock mass may not resist the adjusted high stress after excavation which can lead to rock failure in mining engineering. For example, a serious slabbing failure occurred in a laneway of the Linglong Gold Mine in Shandong Province, China, The cover depth of the laneway is 450 m to earth surface, but the in-situ stress is quite high.

LI et al [3] and GONG et al [4] realized slabbing failure of rocks in laboratory. During the compressive

testing of rock specimens with a height-width ratio of 0.5 under uniaxial compression condition and dimensions of 50 mm × 25 mm × 25 mm under true triaxial unloading condition, slabbing failures were deeply investigated. It was pointed out that the slabbing strength of granite was about 60% of its uniaxial compressive strength [3]. However, the previous studies did not reveal the conditions to induce slabbing fractures in laboratory, and the mechanism of slabbing failure of hard rock in mining sites is still not fully clear. Spalling (or slabbing) failure of hard rock specimens under “high  $\sigma_1$ , moderate  $\sigma_2$ , and low  $\sigma_3$ ” condition was numerically modelled by using FEM/DEM combined numerical tool ELFEN [5]. The study showed that the generation of tunnel surface parallel fractures and micro-cracks was attributed to material heterogeneity and the existence of relatively high intermediate principal stress ( $\sigma_2$ ), as well as zero to low minimum principal stress ( $\sigma_3$ ) confinement [5].

It is worthy to study the rock failure characteristics under high in-situ stresses, including rock slabbing failure. The true triaxial compressive machine can realize the measurement to simulate the high in-situ stresses,

loading and unloading processes [6,7]. Some researchers have carried out experimental studies on rock strength by true triaxial compressive machine. CHANG and HAIMSON [8,9] studied the mechanical properties of rocks and the mechanism of rock burst by true triaxial machine. OKADA et al [10,11] used the self-developed experimental equipment to conduct true triaxial tests on tuff under equally confining pressure.

The foundation of rock mechanics experiment study and theoretical analysis is the experimental observations. The stress environment, strength and deformation failure of rock material are complex and variable because of its anisotropic property. In order to better understand the mechanical properties of rock, observation methods and equipments with the high precision and stability in different external environments are applied in the laboratory tests. The well understanding of the characteristic of rock material can help to ensure the stability of geotechnical engineering and prevent the underground engineering disasters such as rock slabbing. New observation methods are the research topic in rock mechanics and engineering. Acoustic emission (AE) and infrared radiation properties observation methods can provide a new visual angle on rock. HE et al [12] and LEI et al [13] studied the rock failure characteristics under true triaxial loading process by considering the acoustic emission (AE) of rocks. Infrared thermography provides a non-destructive, non-contact and real-time test to observe the physical process of material degradation and to detect the occurrence of intrinsic dissipation without surface contact or in any way influencing the actual surface temperature of the tested object [14,15].

In the present work, true triaxial unloading compression test was carried out by self-developed true-triaxial testing equipment. The relationship between the failure mode and stress state was studied. The AE and infrared radiation characteristics were monitored during the testing. The monitored results show that the failure mode of rock transfers from shear failure to slabbing failure.

## 2 Testing equipment and method

### 2.1 Equipments

The experiments were conducted by self-developed true triaxial testing equipment, which can realize true triaxial loading and dynamic disturbance. The system consists of computer, controllers, actuators, sensors and frames, as shown in Fig. 1. It is a digital closed-loop control system, which can realize controlling of load, deformation and displacement automatically.

The testing equipment can apply load to high stress level in three directions independently ( $\sigma_1 > \sigma_2 > \sigma_3 \neq 0$ ,

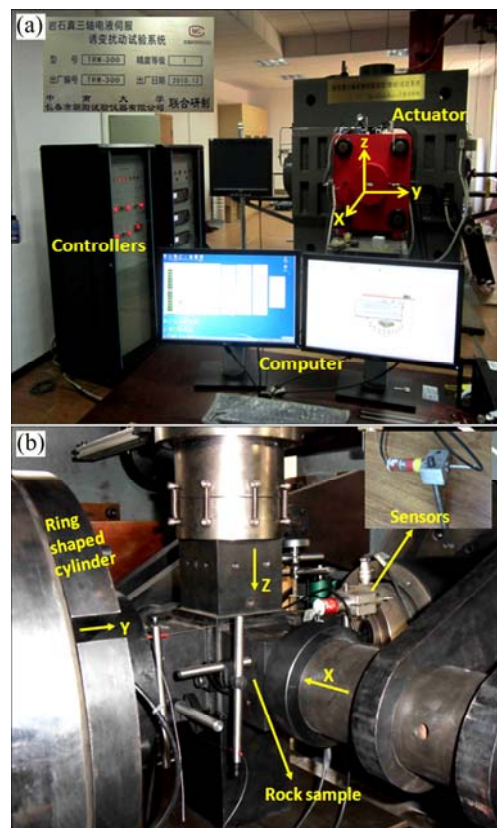


**Fig. 1** True triaxial testing equipment: (a) Overview; (b) Three-direction loading actuators

where  $\sigma_1$  is the maximum principal stress;  $\sigma_2$  is the intermediate principal stress;  $\sigma_3$  is the minimum principal stress). The strength and deformation characteristics of rock under high stress condition can be obtained. Realizing unloading and imposing dynamic load process are the two important functions of the system that are different from other triaxial testing systems. Meanwhile, the machine can realize unloading stresses in one or two directions. The dynamic loads on specimens can be simulated by applying regular or triangle stress waves.

The PCI-2 AE test system was used to monitor the acoustic emission counts of rocks. During tests, the gain of AE event was set to 45 dB and the threshold value was also set to 45 dB, with the sampling frequency of  $10^6$  Hz. ThermoView Pi20 infrared camera was used to measure slight temperature changes of rock specimens during tests. The highest resolution of the ThermoView Pi20 infrared camera can reach  $0.08$  °C at  $30$  °C.

### 2.2 Testing specimens and procedures

Studies on the mechanics properties of rocks under the stress path of underground engineering excavation were carried out. To simulate the stress path of underground engineering excavation process, the proper unloading type should be chosen and applied. According to the engineering practice, four kinds of unloading types

were put forward, as shown in Table 1.

UL 3 is the most common unloading type in underground engineering. So UL 3 was chosen in this work: Unloading  $\sigma_3$ , keeping  $\sigma_2$  and increasing  $\sigma_1$  to the failure strength of rock specimen. Two rocks were used in the tests, which were granite and red sandstone. The granite samples were obtained from a granite quarry in Miluo, Hunan Province, China, and the red sandstone samples were obtained from a quarry in Shandong Province, China. Testing procedures of cubic rock specimens (100 mm×100 mm×100 mm) are as follows:

1) Loading the specimen to predefined geostress level in  $X$ ,  $Y$  and  $Z$  directions. For different rock types, the predefined geostress levels are also different and the predefined geostress levels are listed in Table 2.

Firstly,  $\sigma_1$  was loaded to 0.5 MPa by using displacement control method, i.e.  $F_Z=5$  kN and then  $\sigma_1$  was loaded to 5.0 MPa by using force control method with a loading speed of 2000 N/s (0.2 MPa/s); Secondly,  $\sigma_2$  and  $\sigma_3$  were loaded to 0.5 MPa by using displacement control method, i.e.,  $F_Y=F_X=5$  kN. Afterwards,  $\sigma_1$ ,  $\sigma_2$  and  $\sigma_3$  were loaded to geostress level synchronously by force control method at the speed of 2000 N/s.

2) Unloading  $\sigma_3$  and loading  $\sigma_1$  until specimen failure. When finishing the loading to the predefined geostress level,  $\sigma_3$  was removed suddenly while  $\sigma_1$  increased gradually until rock specimens got final failure. For instance,  $\sigma_3$  was unloaded to 0 immediately, and then  $\sigma_1$  increased at the speed of 2000 N/s until the rock

specimen got final failure.

After unloading of the minimum principle stress  $\sigma_3$ , the AE and infrared heat characteristics were monitored during the testing process.

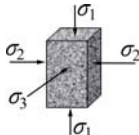
### 3 Testing results and discussion

According to the suggested methods of ISRM (International Society for Rock Mechanics) [16], the standard uniaxial compression test was carried out on two rocks and the uniaxial compressive strengths of granite and red sandstone are 139.0 MPa and 57.87 MPa, respectively. So the granite belongs to a typical hard rock, and the red sandstone belongs to medium hard rock.

#### 3.1 Failure mode

The failure modes of cubic rock specimens were identified by the shape and size of rock failure debris. When the cubic rock specimen is under uniaxial compression or  $\sigma_2=10$  MPa, both ends of cubic rock specimens produce compressive cones and the rock failure mode belongs to shear failure, as shown in Fig. 2(a). When  $\sigma_2=20$  MPa, debris still contains compressive cone but the size of the cone decreases significantly (Fig. 2(c)). When  $\sigma_2=30$  and 40 MPa, the failure mode turns from shear to slabbing, where the compressive cone cannot be observed, as shown in Figs. 2(d) and (e).

**Table 1** Unloading type

Unloading type	Stress state	Unloading process	Corresponding engineering
UL 1		Unloading $\sigma_3$ , keeping $\sigma_1$ and $\sigma_2$	Slope and foundation engineering
UL 2		Successively unloading $\sigma_3$ and $\sigma_2$ , keeping $\sigma_1$	Open pit mining engineering
UL 3		Unloading $\sigma_3$ , keeping $\sigma_2$ , increasing $\sigma_1$	Independent roadway
UL 4		$\sigma_1 > \sigma_2 > \sigma_3 > 0$	Unloading $\sigma_3$ , increasing $\sigma_1$ , unloading $\sigma_2$

**Table 2** Predefined loading stresses for true triaxial test

Material	Specimen group	Minimum principal stress ( $X$ ), $\sigma_3$ /MPa	Intermediate principal stress ( $Y$ ), $\sigma_2$ /MPa	Maximum principal stress ( $Z$ ), $\sigma_1$ /MPa	Remarks
Granite	g-10-1	0	0	50	Uniaxial compression
	g-10-2	5	10	50	Triaxial unloading compression
	g-10-3	10	20	50	Triaxial unloading compression
	g-10-4	20	30	50	Triaxial unloading compression
	g-10-5	30	40	50	Triaxial unloading compression
Red sandstone	s-10-1	0	0	40	Uniaxial compression
	s-10-2	5	10	40	Triaxial unloading compression
	s-10-3	10	20	40	Triaxial unloading compression
	s-10-4	20	30	40	Triaxial unloading compression

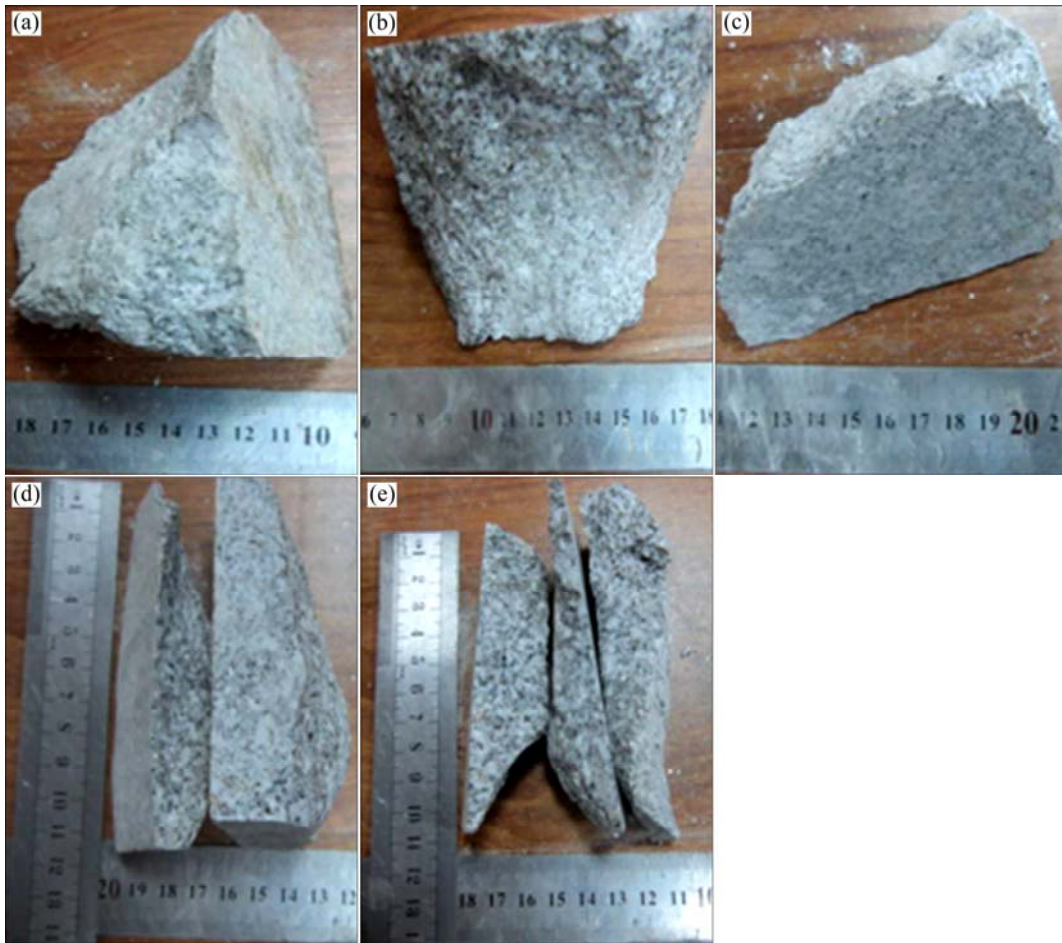


**Fig. 2** Failure mode evolution process of granite specimens under different  $\sigma_2$ : (a)  $\sigma_2=0$ ; (b)  $\sigma_2=10$  MPa; (c)  $\sigma_2=20$  MPa; (d)  $\sigma_2=30$  MPa; (e)  $\sigma_2=40$  MPa

The failure mode of red sandstone specimen is similar to that of granite specimens under true triaxial unloading condition, as shown in Fig. 3. No compressive cone of red sandstone is found when  $\sigma_2=20$  MPa, which is the difference of failure type between granite and red sandstone.

From the above discussion, when  $\sigma_2$  is in a low level ( $\sigma_2 < 20$  MPa), the failure mode of rocks in this work is shear failure, as shown in Fig. 4(a). It can also be concluded that the main cracks of granite and red sandstone specimens under true triaxial unloading condition ( $\sigma_2 \geq 20$  MPa) are parallel to the free surface and the failure mode is slabbing, as shown in Fig. 4(b). Slabbing failure of hard rock specimens was numerically modelled by CAI [5]. The failure process of cubic granite specimens under true triaxial unloading condition ( $\sigma_2 \geq 20$  MPa) can be described as follows: with the increase of  $\sigma_1$ , a series of cracks which are parallel to the free surface firstly generate and propagate in rock specimen. Then, slabbing fractures appear and the spalling phenomenon occurs at the free surface of rock specimen. Afterward, the splitting rock slabs is compressed to final failure.

### 3.2 Strength characteristic

Mohr–Coulomb criterion is a widely used failure criterion for rocks, which supposes that the rock fails in a shear way. Based on the uniaxial compressive test results for cubic rock specimens, the cohesion ( $c$ ) and the internal friction angle ( $\varphi$ ) can be determined from the fracture angle ( $\theta$ ) and uniaxial compressive strength ( $\sigma_c$ ) by using relationships  $\varphi = 2\theta - 90^\circ$  and  $c = \sigma_c(1 - \sin \varphi) / (2 \cos \varphi)$ . For granite,  $c = 36.9$  MPa,  $\varphi = 36^\circ$ ; for red sandstone,  $c = 21.6$  MPa,  $\varphi = 28^\circ$ . The Mohr–Coulomb strength formula can be established by

$$\sigma_1 = \frac{1 + \sin \varphi}{1 - \sin \varphi} \cdot \sigma_3 + \frac{2c \cdot \cos \varphi}{1 - \sin \varphi} \quad (1)$$

Therefore, for granite:  $\sigma_1 = 3.85\sigma_3 + 144.8$ ; for red sandstone:  $\sigma_1 = 1.88\sigma_3 + 71.9$ .

During the true triaxial unloading test, since  $\sigma_3$  was unloaded to 0,  $\sigma_3$  in these formulae should be substituted by  $\sigma_2$ . Previous discussion shows that the failure mode of the granite and red sandstone specimens is changed from shear to slabbing when  $\sigma_2$  increases to a certain value. The tested compressive strength is also different from the



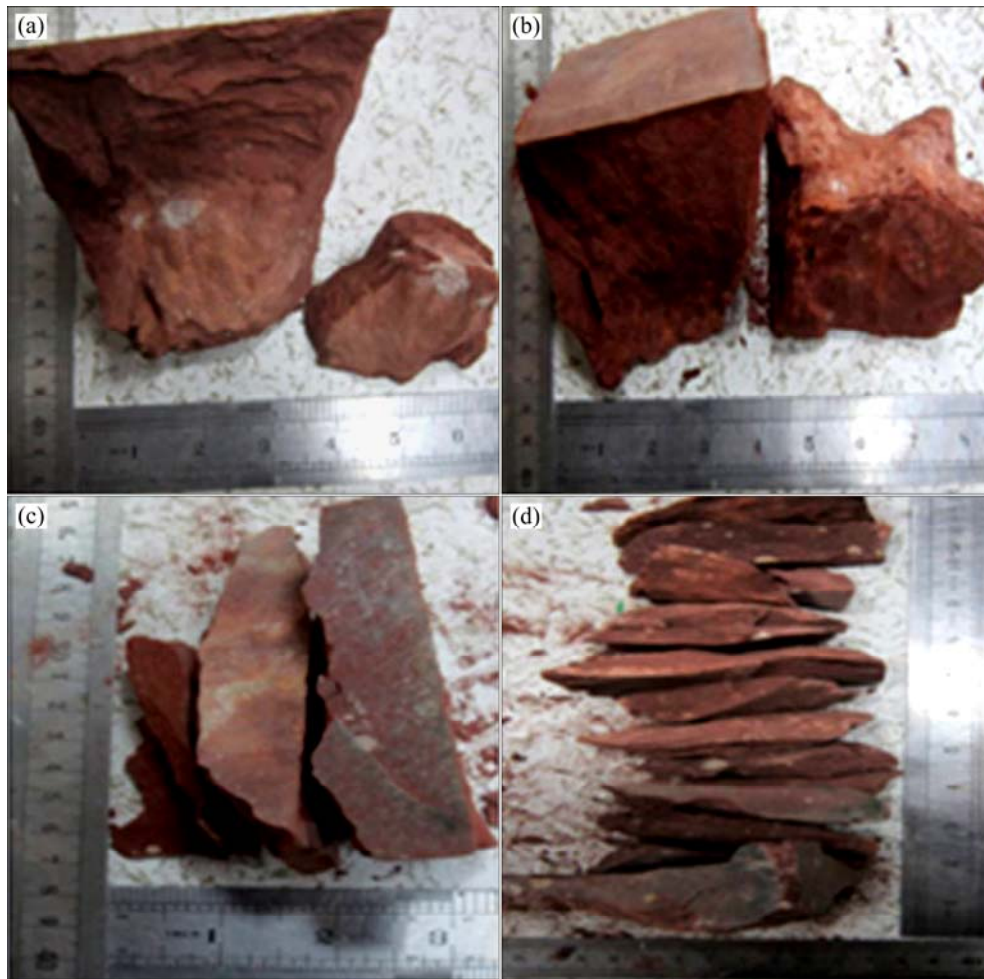


**Fig. 3** Failure mode evolution process of red sandstone specimen under different  $\sigma_2$ : (a)  $\sigma_2=0$ ; (b)  $\sigma_2=10$  MPa (c)  $\sigma_2=20$  MPa; (d)  $\sigma_2=30$  MPa

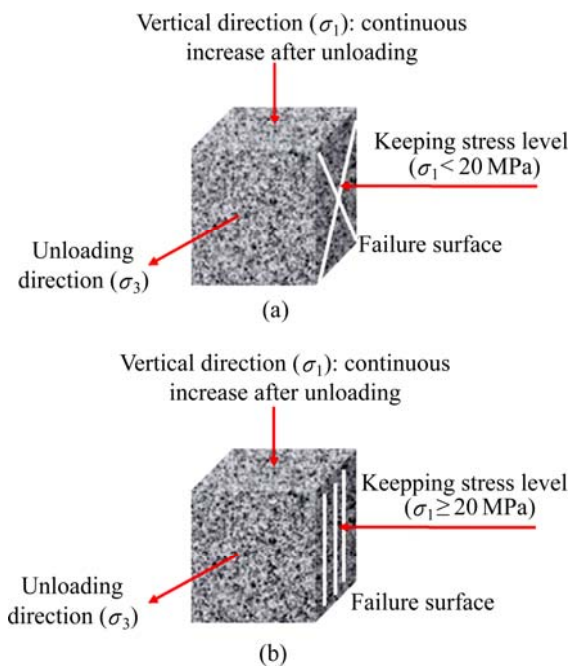


**Fig. 4** Relationship between failure surface and stress state: (a) Shear failure; (b) Slabbing failure

strength value calculated by the Mohr–Coulomb criterion.

The Mohr–Coulomb strength curves and the strengths of these two tested rocks are shown in Fig. 5. From Fig. 5(a), it can be seen that with the increase of  $\sigma_2$ , the strength difference between the calculated strength and the real tested strength also increases. If the failure mode of rock is shear failure, the compressive strength of rock specimen should be equal or close to the strength calculated by Mohr–Coulomb criterion. The difference of the curves implies that the failure mode of rock specimens changes.

### 3.3 AE characteristic

In the loading process (continually loading  $\sigma_1$ ), the AE count rate–time curves and the stress–time curves of granite specimens are shown in Fig. 6. It can be seen that the value of AE count rate decreases with the increase of  $\sigma_2$  during this loading stage. Figures 6(a) and (b) show that the AE count rate keeps at a relatively high level

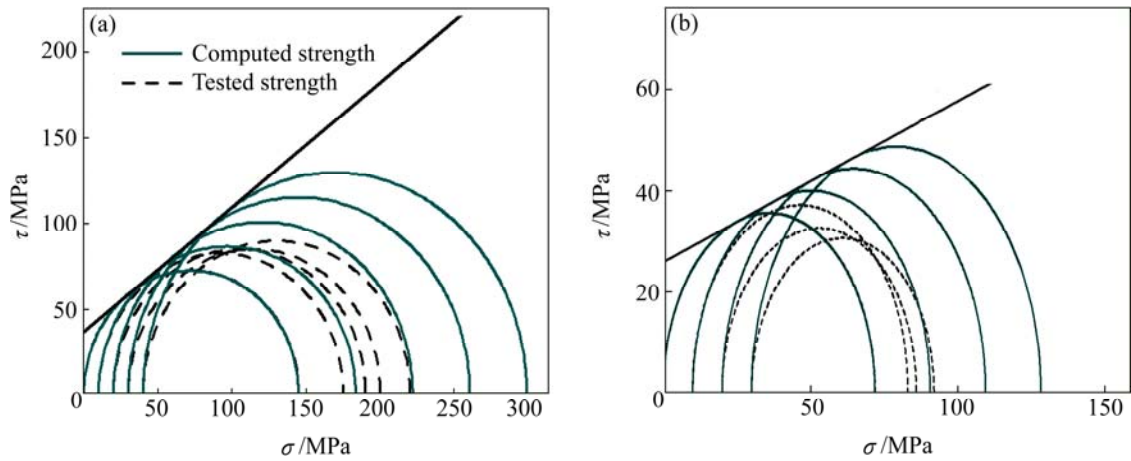


**Fig. 5** Mohr–Coulomb strength curve and Mohr circles: (a) Granite; (b) Red sandstone

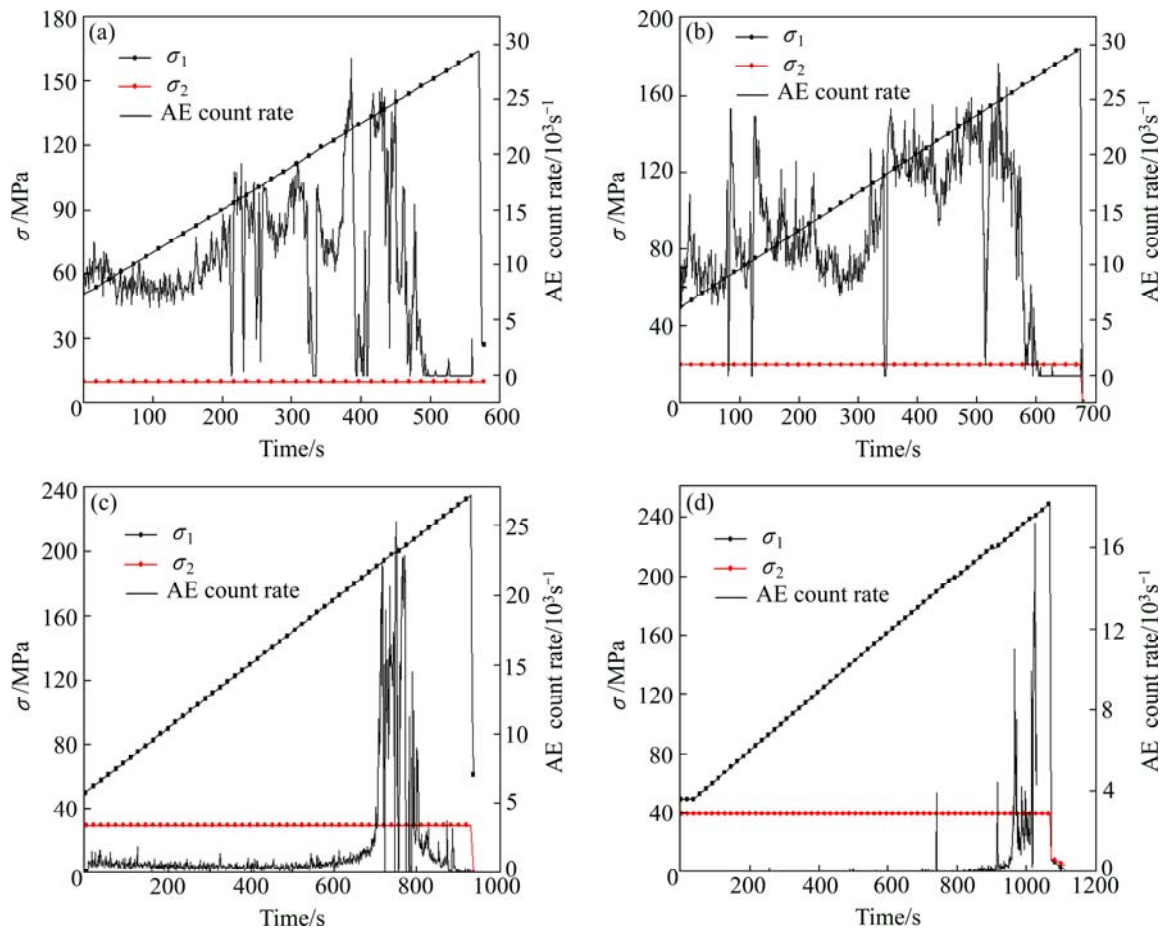


**Fig. 6** AE count rate curves and stress paths of granite specimens: (a)  $\sigma_2=10$  MPa; (b)  $\sigma_2=20$  MPa; (c)  $\sigma_2=30$  MPa; (d)  $\sigma_2=40$  MPa

(more than 10000/s) during the loading process of  $\sigma_1$  when  $\sigma_2$  is equal to 10 and 20 MPa, while AE count rate maintains a much lower level (less than 100/s) and then increases to 10000/s suddenly when  $\sigma_2$  reaches to 30 and 40 MPa, as shown in Figs. 6(c) and (d). When  $\sigma_2$  is less than or equal to 20 MPa, the failure mode of specimen contains shear failure and shear cracks are the main source of AE events. When  $\sigma_2$  is larger than 30 MPa, the

failure mode of specimen belongs to slabbing, and vertical spitting crack leads to the occurrence of AE events. AE count rate can tell what kind of crack leads to rock failure. When  $\sigma_2$  is less than or equal to 20 MPa, shear cracks expand continuously during the loading process of  $\sigma_1$ . When  $\sigma_2$  is larger than 20 MPa, slabbing cracks suddenly propagate when  $\sigma_1$  reaches a certain value.

The red sandstone belongs to medium hard rock. The AE count rate and the stress paths of red sandstone specimens are shown in Fig. 7. When  $\sigma_2=10$  MPa, the AE count rate at the initial loading is high, as shown in Fig. 7(a), which proves that shear cracks are developing in rock specimens. With the increase of  $\sigma_2$ , the lateral confinements are improved and the AE count rate decreases at the initial loading stage. However, when  $\sigma_1$  reaches approximate 80%–90% of the peak strength, AE count rate reaches its maximum value suddenly. It means

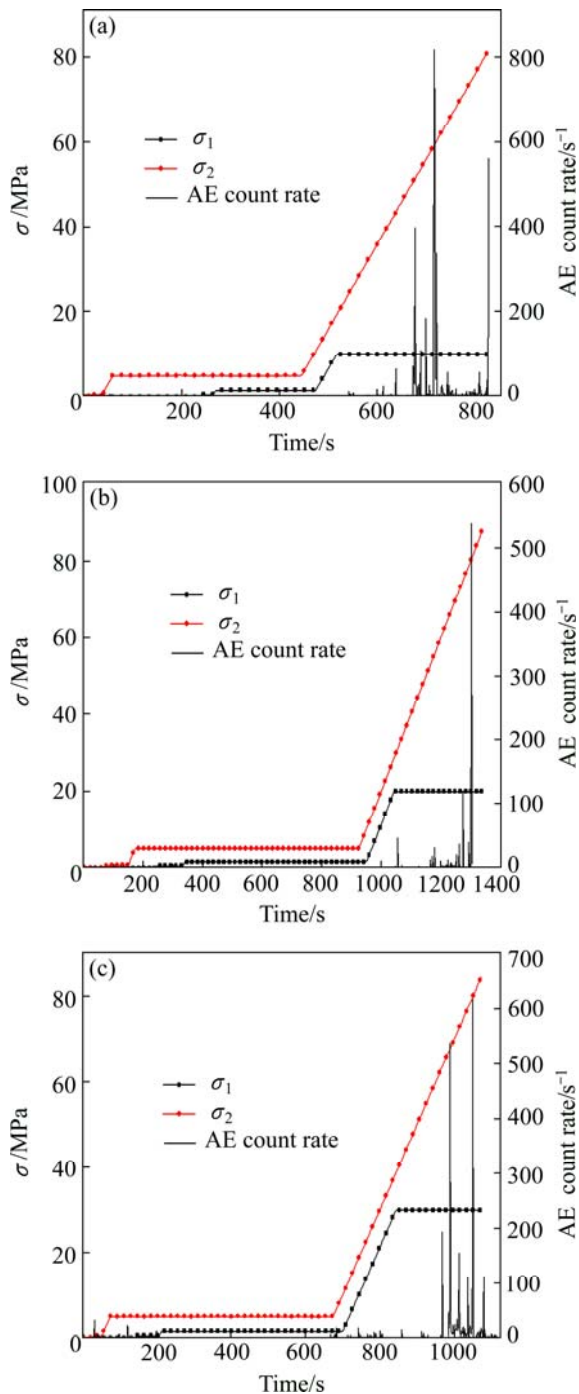


**Fig. 7** AE count rate curves and stress paths of red sandstone specimens: (a)  $\sigma_2=10$  MPa; (b)  $\sigma_2=20$  MPa; (c)  $\sigma_2=30$  MPa

that the slabbing cracks are developing in rock specimens, as shown in Figs. 7(b) and (c).

The AE characteristic of rock specimen under low  $\sigma_2$  is swarm type which is the main shock type under high  $\sigma_2$ . The main reasons are as follows: 1) With the increase of the intermediate principal stress, the crack extension of rock specimen is restricted because the lateral restraint is largened; 2) With the increase of the intermediate principal stress, the triaxial strength of rock specimen increases and the rock specimens will be in early phase of elastic stage with larger  $\sigma_2$  and the number of AE events decreases; 3) The failure mode changes under high  $\sigma_2$ .

### 3.4 Infrared radiation properties

Through ThermoView Pi20 infrared camera, the infrared radiation properties of rock specimens under true triaxial unloading compression test are monitored. Several observation frames are marked on the surface of specimens with label of AOI-01, AOI-02 and AOI-03, as shown in Figs. 8 and 9.

Figure 8 shows the temperature of granite specimens with different  $\sigma_2$  during the compressive progress. The average temperature of rock specimen is 16.2 °C before failure under uniaxial compressive test and it reaches about 26 °C when rock failure occurs. The temperature increases by 9.8 °C. The temperature change area is just along the shear fracture. It proves that the failure mode of cubic rock specimen under uniaxial compression should belong to shear failure. When  $\sigma_2$  increases to 20 MPa, the lower part of specimen firstly gets breaking. The temperatures in the area of AOI-01 and AOI-02 do not change, but the temperature in the area of AOI-03 increases from 12.4 °C to 14.2 °C. The failure mode changes from shear to slabbing gradually. When the specimen is tested with  $\sigma_2=40$  MPa, the temperatures of rock specimen in the areas of AOI-01, AOI-02 and AOI-03 change from 13.8 °C to 19.1 °C, from 13.7 °C to 22.4 °C and from 13.5 °C to 20.9 °C, respectively, before and after failure. The failure surface is planar and the failure mode belongs to slabbing failure. The temperatures of rock specimens under different stress states are listed in Table 3.

Figure 9 shows the temperature of red sandstone specimens with different  $\sigma_2$  during the compressive progress. The average temperature of AOI-01 is 14.7 °C before failure under uniaxial compressive test and it reaches 17.3 °C when rock failure occurs. The temperature change area is just along the shear fracture. The failure mode of cubic red sandstone specimen under uniaxial compression is shear failure. When  $\sigma_2$  increases to 10 MPa, the lower part of specimen firstly gets breaking



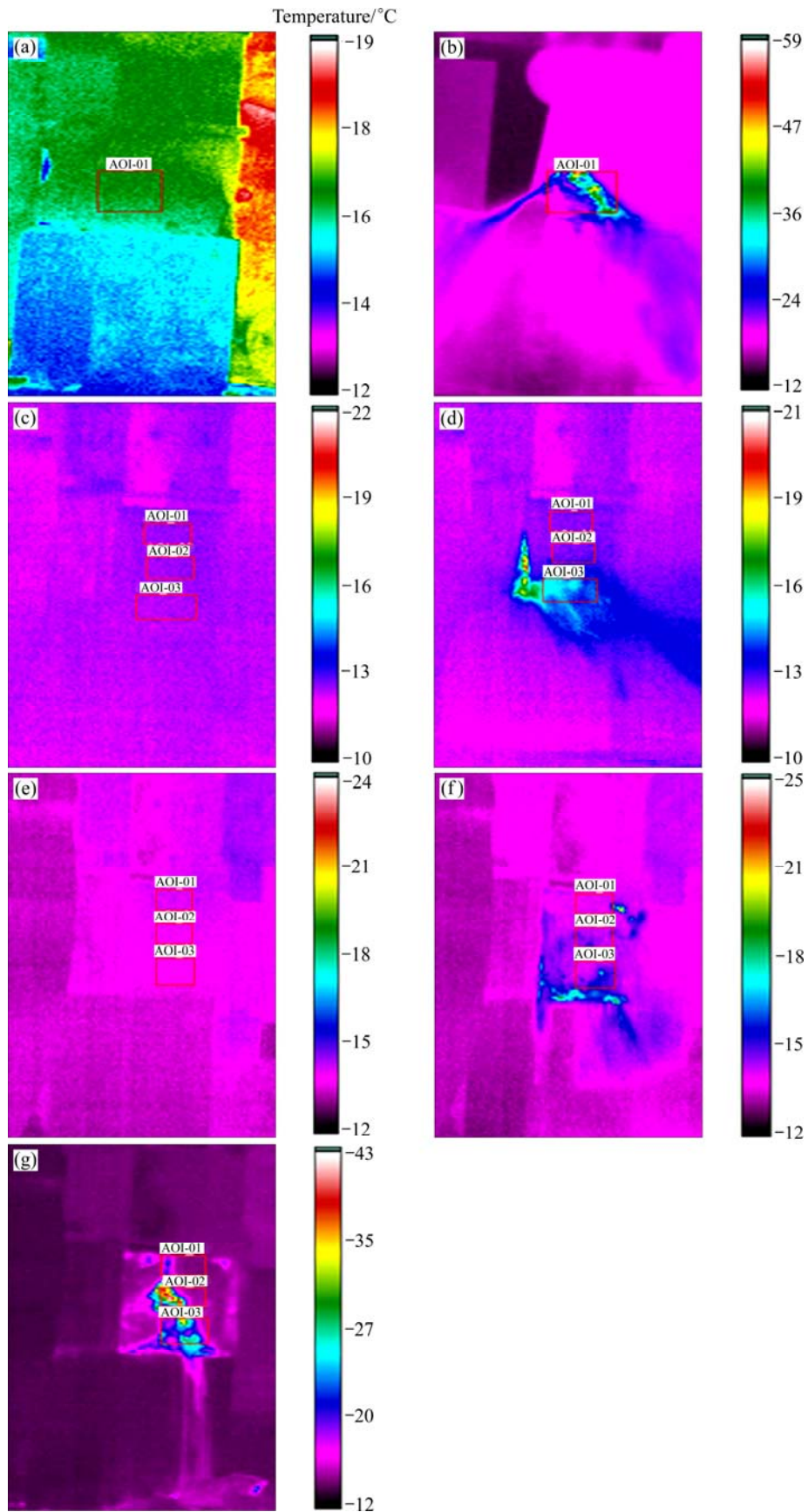


**Fig. 8** Temperature contours of granite specimens with different  $\sigma_2$ : Specimen g-10-1 before (a) and after (b) failure with  $\sigma_2=0$  MPa; Specimen g-10-3 before (c) and after (d) failure with  $\sigma_2=20$  MPa; Specimen g-10-5 before (e) and after (f) slabbing failure and after complete failure (g) with  $\sigma_2=40$  MPa



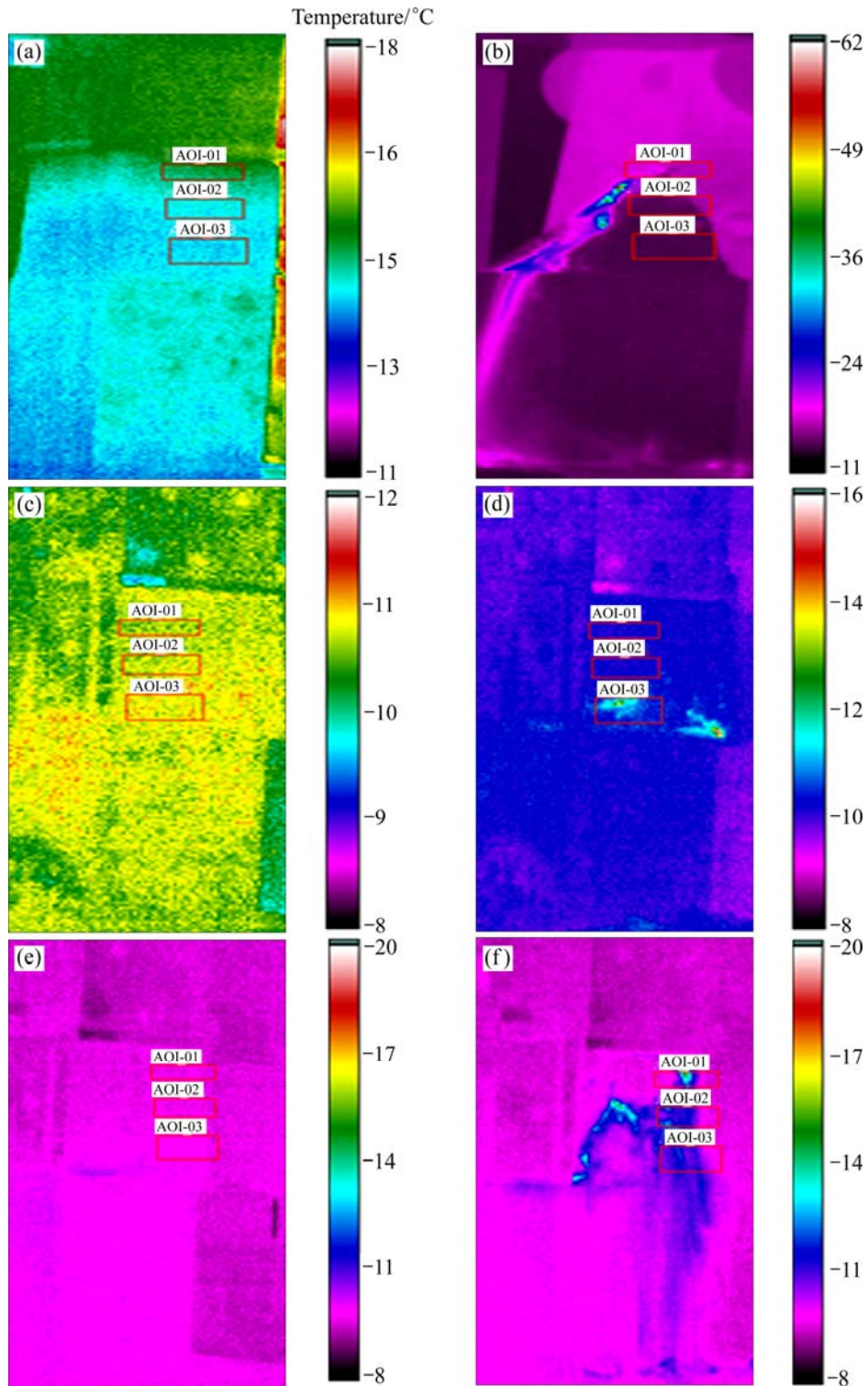


**Fig. 9** Temperature contours of red sandstone specimens with different  $\sigma_2$ : Specimen s-10-1 before (a) and after (b) failure with  $\sigma_2=0$  MPa; Specimen s-10-2 before (c) and after (d) failure with  $\sigma_2=10$  MPa; Specimen s-10-4 before slabbing failure (e) and after complete failure (f) with  $\sigma_2=30$  MPa

and the temperature in the area of AOI-03 increases from 10.6 °C to 11.0 °C. The failure mode changes to slabbing. When the specimen is tested at  $\sigma_2=30$  MPa, the temperature of rock specimen in the areas of AOI-01, AOI-02 and AOI-03 changes from 9.5 °C to 10.3 °C,

from 9.5 °C to 10.6 °C and from 9.6 °C to 10.6 °C before and after failure, respectively. The failure surface is planar and the failure mode belongs to slabbing failure. The temperatures of rock specimens under different stress states are listed in Table 4.

**Table 3** Temperature of granite specimen under different stress states

Specimen No.	Time*	$\sigma_2$ /MPa	Position	Min temperature/°C	Average temperature/°C	Max temperature/°C
g-10-1	1	0	AOI-01	15.8	16.2	16.6
	3			17.5	26	58.8
g-10-2	1	20	AOI-01	12.3	12.5	12.8
	3			12.2	12.5	12.7
	1		AOI-02	12.3	12.5	12.8
	3			12.2	12.6	13.1
	1		AOI-03	12.2	12.4	12.7
	3			13.4	14.2	15.2
g-10-3	1	40	AOI-01	13.7	13.8	14.0
	2			13.7	14.0	15.6
	3			13.7	19.1	35.7
	1		AOI-02	13.5	13.7	13.9
	2			13.9	14.4	15.2
	3			14.2	22.4	41.8
	1		AOI-03	13.2	13.5	13.7
	2			13.9	14.6	17.6
	3			14.7	20.9	36.5

\* “1” represents the temperature measured time before the failure of rock specimen; “2” represents the temperature measured time just at the failure point of rock specimen; and “3” represents the measured time that the temperature of rock specimen reaches its maximum value during the test.

**Table 4** Temperature of red sandstone specimen under different stress states

Specimen No.	Time*	$\sigma_2$ /MPa	Position	Min temperature/°C	Average temperature/°C	Max temperature/°C
s-10-1	1	0	AOI-01	14.4	14.7	15.0
	3			15.2	17.3	19.9
	1		AOI-02	13.9	14.1	14.3
	3			14.0	14.8	16.7
	1		AOI-03	13.8	14.0	14.2
	3			13.8	14.0	14.3
s-10-2	1	10	AOI-01	10.2	10.4	10.6
	3			10.2	10.4	10.6
	1		AOI-02	10.3	10.5	10.7
	3			10.3	10.5	10.7
	1		AOI-03	10.3	10.6	10.8
	3			10.4	11.0	13.6
s-10-4	1	30	AOI-01	9.3	9.5	9.7
	3			9.3	10.3	14.5
	1		AOI-02	9.2	9.5	9.7
	3			9.2	10.6	12.3
	1		AOI-03	9.1	9.6	9.9
	3			9.3	10.6	11.9

\* “1” represents the temperature measured time before the failure of rock specimen; “3” represents the measured time that the temperature of rock specimen reaches its maximum value during the test.

## 4 Conclusions

1) The failure mode of hard rock is affected by the intermediate principle stress  $\sigma_2$ . When  $\sigma_2$  is larger than

20 MPa for the tested two rocks, the failure mode of hard rock might change from shear to slabbing under the true triaxial unloading condition.

2) With the increase of  $\sigma_2$ , the crack extension of rock specimen is restricted and the AE count rate

becomes less during loading  $\sigma_1$ . The AE count rate increases suddenly when slabbing cracks occurs. Since it lacks of precursor information for the occurrence of slabbing fractures, it implies that slabbing failure (like rock burst) of hard rock is not easy to predict by AE methods in mining sites. The next key research points can be concentrated on the prevention and treatment of slabbing failure in hard rock mine.

3) The temperature distribution on rock specimen surface is different for different failure modes such as slabbing and shear. The surface temperature change of cubic rock specimen under uniaxial compression is conical and its failure mode is shear. With the increase of  $\sigma_2$ , the temperature change area is also the failure surface which is planar and the failure mode turns into slabbing.

## References

- [1] LI Xi-bing, YAO Jin-rui, GONG Feng-qiang. Dynamic problems in deep exploitation of hard rock metal mines [J]. The Chinese Journal of Nonferrous Metals, 2006, 21(10), 2551–2563. (in Chinese)
- [2] BROWN E T, BRADY B H G. Trends in relationships between measured in situ stresses and depth [J]. International Journal of Rock Mechanics and Mining Sciences, 1978, 15(6): 211–215.
- [3] LI Di-yuan, LI C, LI Xi-bing. Influence of sample height-to-width ratios on failure mode for rectangular prism samples of hard rock loaded in uniaxial compression [J]. Rock Mechanics and Rock Engineering, 2011, 44(3): 253–267.
- [4] GONG Q M, YIN L J, WU S Y, ZHAO J, TING Y. Rock burst and slabbing failure and its influence on TBM excavation at headrace tunnels in Jinping II hydropower station [J]. Engineering Geology, 2012, 124: 98–108.
- [5] CAI M. Influence of intermediate principal stress on rock fracturing and strength near excavation boundaries—Insight from numerical modeling [J]. International Journal of Rock Mechanics and Mining Sciences, 2008, 45(5): 763–772.
- [6] HAIMSON B. True triaxial stresses and the brittle fracture of rock [J]. Pure Appl Geophys, 2006, 163: 1101–1130.
- [7] IBSEN LB, PRAASTRUP U. The Danish rigid boundary true triaxial apparatus for soil testing [J]. Geotech Test, 2002, 25: 1–12.
- [8] CHANG C, HAIMSON B C. True triaxial strength and deformability of the KTB deep hole amphibolite [J]. Journal of Geophysical Research, 2000, 105 (8): 18–999.
- [9] HAIMSON B C, CHANG C. True triaxial strength of KTB amphibolite under borehole wall conditions and its use to estimate the maximum horizontal in-situ stress [J]. Journal of Geophysical Research, 2002, 107(B10): 2–257.
- [10] OKADA T, TANI K, KANATANI M. Development of in-situ triaxial test for inhomogeneous rock mass [J]. Tsuchi-to-Kiso, 2006, 54(4): 22–24.
- [11] OKADA T, TANI K, OOTSU H. Development of in-situ triaxial test for rock masses [J]. International Journal of Japanese Committee for Rock Mechanics, 2006, 2(1): 7–12.
- [12] HE M C, MIAO J L, FENG J L. Rock burst process of limestone and its acoustic emission characteristics under true-triaxial unloading conditions [J]. International Journal of Rock Mechanics and Mining Sciences, 2010, 47(2): 286–298.
- [13] LEI Xing-lin, MASUDA K, NISHIZAWA O, JOUNIAUX L, LIU Li-qiang, MA Wen-tao, SATOH T, KUSUNOSE K. Detailed analysis of acoustic emission activity during catastrophic fracture of faults in rock [J]. Journal of Structural Geology, 2004, 26(2): 247–258.
- [14] LONG M P. Infrared thermographic scanning of fatigue in metals [J]. Nucl Eng Des, 1995, 158: 363–376.
- [15] ZHANG Yong-jun, AN Li-qian, REN Run-hou, et al. Experimental study of deformation of surrounding rock with infrared radiation [J]. J China Univ of Mining & Tech, 2005, 15(4): 329–333.
- [16] BIENIAWSKI Z T, BERNEDE M J. Suggested methods for determining the uniaxial compressive strength and deformability of rock materials: Part 1. Suggested method for determining deformability of rock materials in uniaxial compression [J]. International Journal of Rock Mechanics and Mining Sciences & Geomechanics Abstracts, 1979, 16(2): 138–140.

## 真三轴卸载试验中岩石的破裂特性

杜坤<sup>1</sup>, 李夕兵<sup>2</sup>, 李地元<sup>2</sup>, 翁磊<sup>2</sup>

1. 中南大学 高等研究中心, 长沙 410083;
2. 中南大学 资源与安全工程学院, 长沙 410083

**摘要:** 深埋地下工程围岩常出现板裂化破坏, 而对于板裂破坏的机理尚不明确。考虑到工程开挖卸载的应力路径, 即“卸载最小主应力, 保持中间主应力, 增大最大主应力”, 为了揭示中间主应力对岩石板裂破坏的影响, 开展真三轴卸载岩石压缩试验。通过监测试验过程中岩石试件的声发射和红外热辐射特性, 分析岩石板裂破坏的发生和发展。试验结果表明: 随着中间主应力的增大, 岩石的破坏模式逐渐由剪切破坏转变为板裂破坏。当中间主应力较小时, 岩石的声发射为群震型; 而当中间主应力较大时, 岩石的声发射为主震型。在不同的中间主应力下, 岩石的红外热辐射特性也不同。当中间主应力较小时, 岩石试件的临空面上温度变化区域为剪切面, 当中间主应力较大时, 温度变化区域为岩石的整个临空面, 进一步证明了岩石的破坏模式转变为板裂破坏。

**关键词:** 真三轴应力; 卸载; 板裂破坏; 声发射; 红外热辐射

(Edited by Yun-bin HE)